Ocean Science
Discussions

The role of turbulence and internal waves in the structure and evolution of a near-field river plume

Rebecca A. McPherson[1], Craig L. Stevens[1,2], Joanne M. O'Callaghan[2], Andrew J. Lucas[3], and Jonathan D. Nash[4]

[1]Department of Physics, University of Auckland, Auckland, New Zealand
[2]National Institute of Water and Atmospheric Research, Wellington, New Zealand
[3]Scripps Institution of Oceanography, University of California San Diego, USA
[4]College of Earth, Oceans and Atmospheric Sciences, Oregon State University, USA

Correspondence: Rebecca A. McPherson (rmcp393@aucklanduni.ac.nz)

Abstract. An along-channel momentum budget is quantified in the near-field plume region of a controlled river flow entering Doubtful Sound, New Zealand. Observations include highly resolved density, velocity and turbulence, enabling a momentum budget to be constructed over a control volume. Estimates of internal stress (τ) were made from direct measurements of turbulence dissipation rates (ϵ) using vertical microstructure profiles. High flow speeds of the surface plume over $2 \ \mathrm{ms^{-1}}$ and strong stratification ($N^2 \sim 10^{-1} \ \mathrm{s^{-2}}$) resulted in enhanced turbulence dissipation rates ($\epsilon > 10^{-3} \ \mathrm{Wkg^{-1}}$) and internal stress ($\tau > 10^{-2} \ \mathrm{m^2 s^{-2}}$) at the base of surface layer. An observed transition from a supercritical to sub-critical flow regime in the initial 1 km indicates the presence of an internal hydraulic jump and the subsequent release of internal gravity waves. The momentum flux divergence of these internal waves suggests that almost 15% of the total plume momentum can be transported out of the system by wave radiation, therefore playing a crucial role in the redistribution of momentum within the near-field plume. Observations illustrate that the evolution of the momentum budget components vary between the distinct surface plume layer and the turbulent, shear-stratified interfacial layer. Within the surface plume, a momentum balance was achieved. The dynamical balance demonstrates that the deceleration of the plume, driven by along-channel advection, is controlled by turbulence stress from the plume discharge point to as far as 3 km downstream. In the interfacial layer however, the momentum equation was dominated by the turbulence stress term and the balance was not closed. The redistribution of momentum within the shear-stratified layer by the observed hydraulic jump and internal wave radiation could account for the discrepancy in the budget.

1 Introduction

The fate of the freshwater, terrigenous material and energy injected into the coastal ocean by river plumes is determined by the initial plume structure, close to the river mouth (McCabe et al., 2009). After the initial discharge at the source, the momentum-

dominated jet-like inflow then evolves into a buoyancy-forced plume in the near-field region (Hetland, 2005). In this near-field region, the structure and behaviour of the plume are determined by a balance of governing plume dynamics, dominated by lateral spreading and vertical mixing. These processes are capable of modifying the density structure and momentum of the flow (Hetland, 2012; MacDonald and Chen, 2004). The plume then propagates through the mid-field region where inflow

25   momentum is lost before transitioning into the far-field. Characterising how the freshwater inflow interacts with the coastal ambient in the near-field region thus underpins the structure of the far-field plume.

     As the plume exits the river mouth and enters the coastal ocean, the strong density gradient between the freshwater plume and ambient coastal water results in a buoyancy-driven lateral spreading of the plume (Hetland, 2012). The surface plume layer thins and accelerates which enhances shear at the plume base, leading to shear-instabilities and turbulence. However,

30   the mixing of low-momentum, high density ambient water into the plume decelerates the flow and reduces shear which leads to a decrease in the density anomaly, thus slowing lateral spreading (Kilcher et al., 2012; MacDonald and Chen, 2004). An understanding of the interplay between these near-field dynamics is necessary to characterise local plume behaviour, determine plume evolution and understand the implications for the larger coastal ocean.

     In order to evaluate the spatial evolution of the plume, measured quantities are connected to plume dynamics by constructing

35   a momentum budget over a defined finite region of the flow field, termed a control volume. The control volume method has been applied to riverine systems to estimate turbulent transport quantities (MacDonald and Geyer, 2004; Chen and MacDonald, 2006), examine plume spreading (MacDonald et al., 2007), and determine the role of mixing in the near-field plume region (McCabe et al., 2008; MacDonald et al., 2013). The role of turbulence in influencing plume structure is generally examined by using control volume methods to estimate turbulence stress (τ) either indirectly as a residual of the budget components

40   (MacDonald and Geyer, 2004) or directly using microstructure profiles (Kilcher et al., 2012). While reasonable agreement between indirect control volume estimates of turbulence stress divergence and direct measurements from shear probes has been found (MacDonald et al., 2007), Kilcher et al. (2012) found discrepancies between indirectly inferred and directly measured τ using an extensive data set, which indicates either under-sampling or errors in the control volume method assumptions. In the present study, τ is derived from vertical microstructure profiles.

45   The turbulence in the near-field region of the river plume system studied in this paper was investigated by McPherson et al. (2019), using direct turbulence measurements from microstructure profilers to examine the drivers of turbulent kinetic energy (TKE) dissipation rate (ϵ) variability within the plume. In the initial 0.5 km downstream of the plume discharge point, measurements of ϵ in the surface plume layer were amongst the highest recorded in oceanic shear flows (maximum $\epsilon > 10^{-2}$ Wkg^{-1}), with ϵ decreasing with distance from the source. To illustrate the impact of these intense rates of turbulent mixing

50   both on the overall structure and behaviour of the plume, and the balance of other governing near-field plume dynamics, a momentum budget over the region can be constructed.

     Internal waves can impact the balance of plume dynamics as they carry mass and energy away from the plume front, and facilitate vertical mixing offshore (Pan and Jay, 2009; Kilcher et al., 2010). Internal hydraulics are classified by the internal Froude number ($Fr_i = u_s/c$), where u_s is the surface speed and $c = \sqrt{g'h}$ is the internal wave speed, g' is the reduced gravity

55   and h is the depth of the surface layer, which sets the criterion for free wave propagation at a plume front. Internal waves are

released when the flow transitions from a supercritical ($Fr_i > 1$) to a sub-critical flow regime ($Fr_i < 1$) (Jay et al., 2009). For example, in the Columbia River, packets of internal waves released from the plume front have been observed to carry up to 70 % of the total energy out beyond the Columbia River's boundaries (Pan and Jay, 2009) and extend the influence of the plume far beyond its bounding front (Nash and Moum, 2005). The transition from supercritical to sub-critical flow can also induce

60 a hydraulic jump which, due to the need to conserve momentum, is highly dissipative (Weber, 2001) and can subsequently release internal waves (Osadchiev, 2018). This conservation of momentum necessarily creates a system that has dissipative losses, thus constructing a momentum balance is the key to understanding the mixing and energy dissipation.

A useful system in which to examine these mechanics are fjords because the deep, narrow basin acts as a large-scale natural laboratory. When a riverine inflow is discharged into the head of the fjord (Pickard and Stanton, 1980), this provides an idealised

65 domain in which to isolate specific aspects of near-field plume dynamics. While the deep bathymetry minimises tidal exchange and the inner basin is sheltered from large ocean swell, fjord-river interactions can been directly applied to coastal plumes as the two systems share many common features: freshwater inflow to the fjord produces similar density gradients observed in major rivers such as the Hudson and Columbia Rivers (MacDonald and Geyer, 2004; Hunter et al., 2010); comparable estimates of ϵ occur in each of the near-field plume regions (MacDonald et al., 2007; McPherson et al., 2019); and time-

70 variable discharge rates, common to both systems, similarly impact the plume structure and energetics (Yankovsky, 2001; O'Callaghan and Stevens, 2015).

The objective of this paper is to quantify the along-channel momentum budget in the near-field region of a river plume using high-resolution observations of velocity, density and turbulence. A control volume is used to relate the measured quantities to the budget components, and the balance of plume dynamics within the plume, interfacial layer and ambient below are

75 examined. The effect of the dynamical balance on plume structure and behaviour is also described. This includes quantifying the role that internal waves and internal hydraulic jumps play in the distribution of energy within the near-field region.

2   Field setting and Data

A controlled freshwater discharge is carried from alpine Lakes Manapouri and Te Anau through the Manapouri hydroelectric power station and, via a constructed channel, into the head of Doubtful Sound, located on the south-west coast of New Zealand

80 (45.3 ° S, 167 ° E) (Fig. 1a,b). Freshwater is discharged at an average flow rate of $Q = 420$ m^{3}s^{-1} with maximum $Q = 550$ m^{3}s^{-1}, making it the third largest river flow in New Zealand (Bowman et al., 1999). Maximum plume speeds, which exceed 2 ms^{-1}, are comparable to the peak ebb outflow velocity of larger river systems such as the Columbia River ($Q > 7,000$ m^{3}s^{-1}) (McCabe et al., 2008).

The main fjord is approximately 35 km long, typically less than 1 km wide and has a maximum depth of 450 m south of

85 Secretary Island (Fig. 1b). The freshwater tailrace is discharged into the head of the inner fjord, Deep Cove (Fig. 1c). Deep Cove is 3.6 km long and, flanked by steep topography, has a maximum depth of 126 m that occurs within 50 m of the shoreline. The exposure of the Fiordland region to prevailing Westerly weather systems and orographic precipitation compounds in annual rainfall in excess of 7 m (Bowman et al., 1999). The tides are predominantly semidiurnal with ranges of 1.5 m and 2.5 m
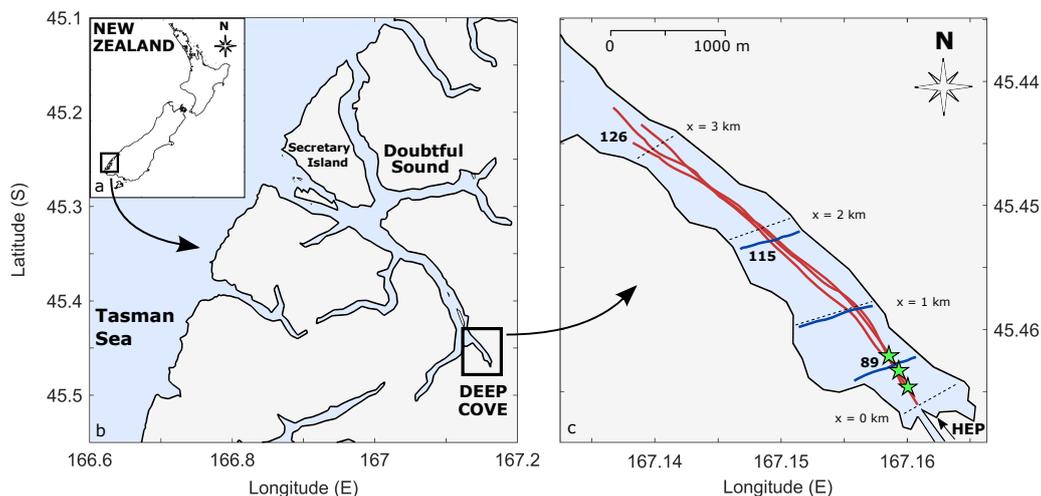
Figure 1. Location map of (a) New Zealand with the Fiordland region highlighted, (b) Doubtful Sound identifying the location of (c) Deep Cove showing the repeated across-channel (blue) and along-channel (red) vessel transects taken on three separate days. The sampling started at the tailrace exit point and continued towards the seaward end of Deep Cove. The mooring locations (stars) are shown. The arrow in (b) indicates the tailrace inflow from the Manapouri hydroelectric power station (HEP) discharged into the head of Deep Cove. The dashed lines across the fjord are reference distances from the tailrace discharge point ($x = 1, 2, 3$ km).

for neap and spring tides respectively (Walters et al., 2001). Observational experiments were conducted between the tailrace

90   discharge point and the seaward end of Deep Cove, approximately 3 km downstream (Fig. 1c).

A two-week field campaign was conducted in March 2016 when tailrace inflow rates were high and relatively steady ($Q \approx$ 530 m^{3}s^{-1}) and wind speeds were typically less than 10 ms^{-1} (Fig. 2). Though wind mixing generates variability in river plumes (Kakoulaki et al., 2014), it has the greatest effect on plume structure in the far-field (Hetland, 2005) thus wind effects shall not be examined here.

95   ## 2.1   Moored timeseries data

A near-surface instrumented mooring array was deployed in the near-field region of Deep Cove (Fig. 1c). The location and configuration of the moorings were determined by results from previous field campaigns in Deep Cove (O'Callaghan and Stevens, 2015; McPherson et al., 2019). Surface velocity was measured by Acoustic Doppler Velocimeters (Nortek Vector) mounted on surface buoys orientated into the seawards-flowing plume and sampled continuously at 1 Hz. The moorings

100   also included temperature loggers (SBE56) sampling at 1 Hz, conductivity-temperature-depth loggers (CTD, SBE37) which sampled every 10 seconds, and an upwards-facing Acoustic Doppler Current Profiler (ADCP; RDI Workhorse 600 kHz) set to record an ensemble every 3 minutes in 2 m vertical bins.

Ocean Science
Discussions
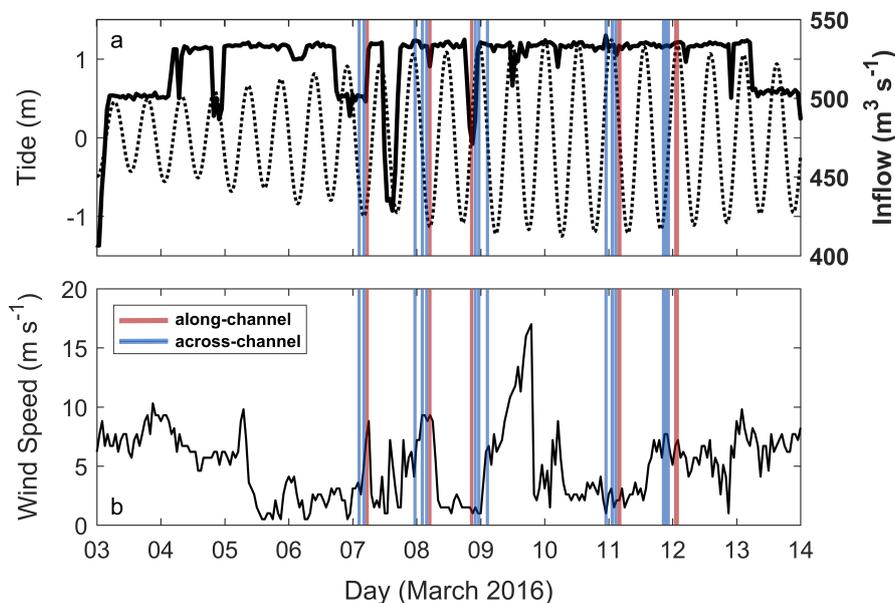
Figure 2. Boundary conditions for the duration of the March 2016 experiment. (a) Discharge from the Manapouri hydroelectric power station (solid) and tides (dotted), and (b) wind speed recorded at the head of Deep Cove. Periods of along-channel (red) and across-channel (blue) transects are indicated.

2.2 Vessel-based survey of currents and density field

Along-channel and across-channel vessel transects, aligned with, and perpendicular to, the main river discharge respectively,
105 were repeated over the course of the field campaign (Fig. 1c). The along-channel transects represented the path of the mean flow as the vessel drifted with the seawards-propagating plume. Data were collected to obtain a spatial distribution of density, velocity and turbulence fields within Deep Cove (Table 1). A weighted bowchain attached to the vessel was comprised of continuously sampling temperature (RBRsolo) and CTD loggers (RBRconcerto) and high-resolution profiles of practical salinity and temperature were obtained from 'tow-yoed' CTD loggers (RBRconcerto) (Fig. 3). These data enabled estimation of the
110 buoyancy frequency from the gradient of the measured density profiles,

$$N = \sqrt{-\frac{g}{\rho}\frac{\partial \rho}{\partial z}} \qquad (1)$$

where ρ is the potential density.

Using the tow-yoed CTD, the vertical momentum flux for internal gravity waves can be calculated,

$$F_z = <u'w'> \qquad (2)$$

5

Ocean Science
Discussions
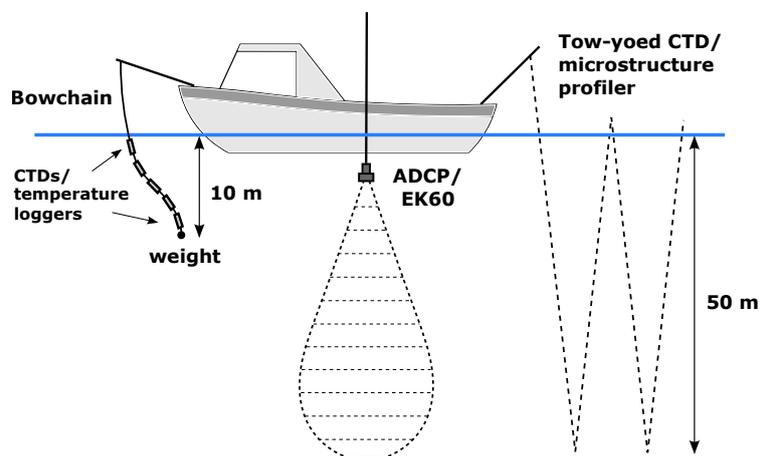
Figure 3. Schematic of vessel-mounted instrumentation set-up including bowchain, pole-mounted ADCP and EK60, tow-yoed CTD and microstructure profiler.

where u' and w' are the horizontal and vertical wave velocities respectively, i.e., the perturbation components after removing the mean flow. The horizontal velocity component (u) is from the vessel-mounted ADCP and the vertical velocity component

115 (w) is calculated using a control volume method (Eqn. 8) which is described in greater detail in Section 2.3. The mean velocity profiles are taken over the total 3 km length of Deep Cove.

A microstructure profiler (VMP 250, Rockland Scientific) was deployed from the side of the vessel, measuring small-scale velocity shear from which estimates of TKE dissipation rates (ϵ) were directly obtained (McPherson et al., 2019). The VMP was deployed in an upwards-profiling mode which enabled measurements right to the water surface. Due to contamination of

120 data by the wake of the instrument, measurements of ϵ towards the bottom of each profile were not always obtained.

Horizontal velocity estimates were obtained from a 600 kHz ADCP (RDI Workhorse) mounted on a pole alongside the vessel 1 m below the surface (Fig. 3). Currents were rotated according to the local bathymetry to determine along-channel (u) and across-channel (v) velocities. Near-surface velocities were obtained by linearly interpolating from the measured ADCP data at 2.5 m to the Velocimeters moored at 0.1 m. The Velocimeter velocity results compared well to estimates of surface

125 currents from a series of Lagrangian GPS drifter experiments in which a pack of surface drifters were released at the tailrace discharge point and, advected with the mean plume flow, retrieved after approximately 1 hour. The surface drifter estimates of plume speed were then applied to determine near-surface velocity towards the seaward end of Deep Cove.

A 600 kHz narrow-beam echosounder (EK60) was also mounted on the other side of the vessel to provide a means of imaging the flow on fine horizontal and vertical scales. The EK60 was positioned 0.5 m below the water surface and measured

130 backscatter in 4.5 cm bins down to 38.5 m (Table 1). Precision position data was obtained from an onboard GPS unit.

Table 1. Summary of Vessel-Mounted Instrumentation[a]

Instrument	Sampling Rate	Depth Range (m)
Tow-Yo CTD	5 Hz	0 - 50
Bowchain CTD	5 Hz	0.5 - 10
Bowchain temperature logger	2 Hz	0.5 - 10
ADCP	600 kHz	2.5 - 41.4
EK60	600 kHz	0.5 - 38.5
VMP-250	512 Hz	0 - 10

Table 2. [a]The tow-yoed CTD was continuously profiled with a fall rate of $\sim 1~\mathrm{ms}^{-1}$. The bowchain was comprised of temperature loggers and CTDs spaced 0.5 m apart. The 600 kHz ADCP was set to sample water velocity continuously in 1 m vertical bins and the 600 kHz echosounder (EK60) was mounted to measure below the surface 0.5 m which was contaminated by vessel motion.

2.3 Plume momentum

By applying the Boussinesq approximation, the along-channel momentum budget is,

$$\frac{\partial u}{\partial t} + \boldsymbol{u} \cdot \nabla u - fv + \frac{\partial P}{\partial x} + \frac{\partial \tau}{\partial z} = 0 \tag{3}$$

where f is the Coriolis parameter, τ is the horizontal shear stress and P is the reduced pressure which is written as a sum of its baroclinic (P_{bc}) and barotropic (P_η) components,

$$P = P_{bc} + P_\eta = \frac{g}{\rho_0} \int_z^0 \rho dz + g\eta \tag{4}$$

135   and η is the surface displacement. The observations in Table 1 directly resolved most of the terms in Eq. (3). The local acceleration was calculated as the observed rate of change of velocity between consecutive tow-yoed profiles. Within the advection term, the u-component was measured directly using the along-channel velocity, the v-component was assumed to be equal to zero along the plume axis, and the w-component was obtained using a control volume method. The total plume deceleration is then defined as $Du/Dt = \partial u/\partial t + u\frac{\partial u}{\partial x} + w\frac{\partial u}{\partial z}$. The contribution from the Coriolis force was estimated using

140   the northward velocity component and the baroclinic pressure gradient ($\partial P_{bc}/\partial x$) was calculated from the observed density field. The horizontal shear stress (τ) is,

$$\tau = -K_\nu \frac{\partial u}{\partial z}. \tag{5}$$

and was derived from the vertical eddy viscosity,

$$K_\nu = \frac{1}{1 - R_f} \frac{\epsilon}{S^2} \tag{6}$$

where S is the velocity shear and a constant flux Richardson number $R_f = 0.17$ was assumed (MacDonald and Geyer, 2004).
In this study, turbulence stress was estimated using direct measurements of ϵ from the vertical microstructure profiles. This is a
145   development of the control volume technique established by MacDonald and Geyer (2004) to indirectly calculated turbulence
for a momentum budget, and thus more accurately represents the mechanisms of turbulent mixing within the budget.

The remaining components of Eq. (3) were estimated using a control volume method. As the majority of energy was found
in the surface layer (O'Callaghan and Stevens, 2015; McPherson et al., 2019), the upper and lower integration limits were
defined by the depth $0 \leq z \leq 10$ m and along-axis distance $0 < x \leq 3$ km. Across-fjord limits (in the y-direction) were defined
150   by the relative plume width ($b(x)$) determined by the freshwater conservation equation,

$$Q_0 = \int\limits_z^0 u \frac{s_0 - s}{s_0} b \, dz \tag{7}$$

where the total freshwater flux (Q_0) is constant, s_0 is the salinity of the ambient and s is the local salinity. The physical
characteristics of the plume itself (e.g., u, N^2, ϵ, etc.) were determined by averaging over the depth of the surface layer (h),
defined as the distance from $z = 0$ to the depth of the maximum N^2 value for each profile. To fully quantify the advection term
in Eq. (3), the vertical entrainment velocity (w) was calculated using the volume conservation equation,

$$w(z) = \frac{1}{b} \left\langle \frac{\partial}{\partial x} \int\limits_z^0 b u \, dz \right\rangle \tag{8}$$

155   assuming that b does not vary in time. The remaining barotropic component of the pressure gradient was estimated by calcu-
lating η using a Bernoulli equation to incorporate the effects of mixing (MacDonald and Geyer, 2004),

$$\eta = \frac{1}{2g} u^2 + \frac{1}{g} \int\limits_0^x \frac{\partial u}{\partial t} dx. \tag{9}$$

using the interpolated surface velocities from the Velocimeter at $z = 0.1$ m.

3   Results

3.1   Near-field water column structure

160   The complex vertical structure of the upper water column in Deep Cove is illustrated by an along-channel echosounder transect.
The bright acoustic scattering layers result from variations in density stratification and microstructure due to turbulence The

Ocean Science
Discussions

Open Access

EGU
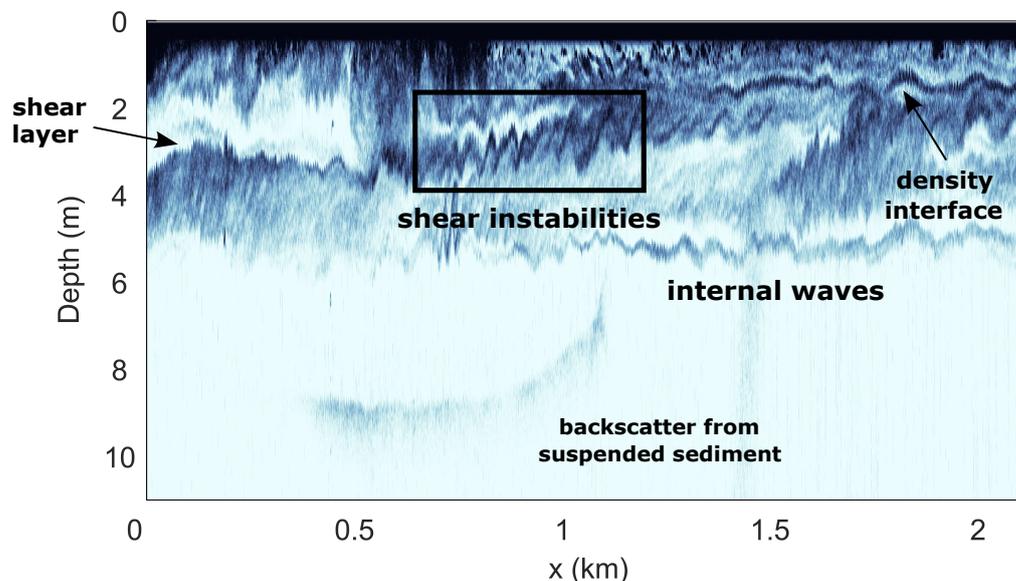
Figure 4. Acoustic backscatter intensity from the echosounder as a function of distance from the tailrace discharge point. The image is coloured so that dark indicates high intensity and white indicates low intensity. The depth of the water column increases from 5 m at the end of the tailrace channel ($x = 0$) to over 90 m in depth over the first 100 m from the tailrace discharge point. The location within the fjord corresponding to the distance axis is shown in Fig. 1c.

transect shows a distinct 5 m deep surface layer in which the scattering intensity is high above a relatively quiescent ambient (Fig. 4). Internal waves can also be seen propagating seawards along the base of the surface layer at 5 m and were not observed to break over the length of Deep Cove.

165   Vertical profiles relate the sounder observations to the physical characteristics of the upper water column (Fig. 5). The surface layer observed in Fig. 4 consisted of a $2 - 3$ m thick freshwater layer flowing at speeds of over 1 ms^{-1} above a sharp density interface (Fig. 5a,b). The quiescent ambient below was of an oceanic density ($\sigma_t \approx 26$ kgm^{-3}) and stationary. The strong backscatter at the base of the surface layer was the salinity-induced stratification in the pycnocline ($N^2 = 10^{-1}$ s^{-2}), and generally weaker N^2 values were observed within the plume layer ($N^2 = 10^{-2}$ s^{-2}), reducing towards 10^{-4} s^{-2} below the

170 interface (Fig. 5c). In the sounder transect, the braided structures approximately 3 m below the water surface with amplitudes between $0.5 - 1$ m (Fig. 4, highlighted box) are indicative of shear instabilities which are a familiar feature in highly stratified shear flows (Tedford et al., 2009; Geyer et al., 2017). These instabilities generated enhanced turbulence at the base of the plume where the billows sustained TKE dissipation rates greater than $\epsilon = 10^{-3}$ Wkg^{-1} close to the discharge point (Fig. 5e).

    The plume spread laterally as it propagated downstream, increasing in width from 105 m at the tailrace discharge point to 240

175 m towards the seaward end of Deep Cove ($db/dx = 0.045$ m^{-1}) (Fig. 6a). The thickness of the surface layer varied spatially, with fluctuations of ~ 1 m over longitudinal distances of less than 100 m (Fig. 6b). The velocity of the plume decreased from
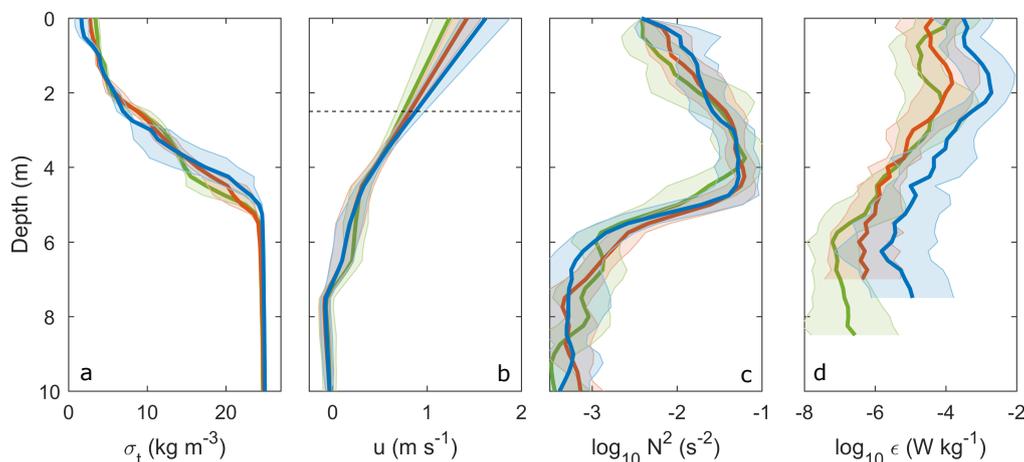
Figure 5. Vertical profiles of (a) sigma-t (σ_t), (b) along-channel velocity (u), (c) stratification (N^2), and (d) turbulence dissipation rate (ϵ) averaged over $0 < x \leq 1$ km (blue), $1 \leq x < 2$ km (orange) and $2 \leq x < 3$ km (green). The horizontal dashed line in (b) shows the depth above which the velocity was interpolated. The shading around each profile represents one standard deviation.

$1.1 - 0.75 \, \mathrm{ms}^{-1}$ over the 3 km (Fig. 6c) and surface layer ϵ and τ also decreased over the length of Deep Cove (Fig. 6e,f). The internal Froude number shows that the flow was initially supercritical ($Fr_i > 1$) and transitioned to a sub-critical flow regime ($Fr_i < 1$) at approximately 1 km downstream from the tailrace discharge point (Fig. 6g).

3.2 Momentum balance evolution

The individual components of the momentum budget (Eq. (3)) were averaged over three 1 km long sections from the tailrace discharge point to the seaward end of Deep Cove. Nearest the tailrace discharge point ($0 \leq x < 1$ km), the along-channel component of advection in the surface layer and a weaker local acceleration term (Fig. 7b) drove strong plume deceleration in the surface layer ($Du/Dt < 0$, Fig. 7c). The error bounds on the advection components relate to the variability in near-surface flow speeds (Fig. 6c). Below the plume at 4 m, Du/Dt tended to zero and the ambient was relatively steady. The spreading component was weak within the plume as w was defined to be zero at the surface (Fig. 7b).

The mean pressure gradient ($\partial P/\partial x$) was the same sign and approximately half the magnitude of Du/Dt within the surface layer (Fig. 7c). The Rossby number, $Ro = u/fL$, where u and L are the mean velocity and width of the river inflow respectively, is $Ro \approx 10^3$ which indicates that the Coriolis force can be neglected. This corresponds to the weak Coriolis force ($10^{-5} \, \mathrm{ms}^{-2}$) relative to the other budget terms in the near-field region (Fig. 7c,g,k). The Coriolis acceleration becomes a primary balancing force in the mid and far-field plume regions (McCabe et al., 2009) and is generally a dominant factor in large-scale systems (Fong and Geyer, 2002).
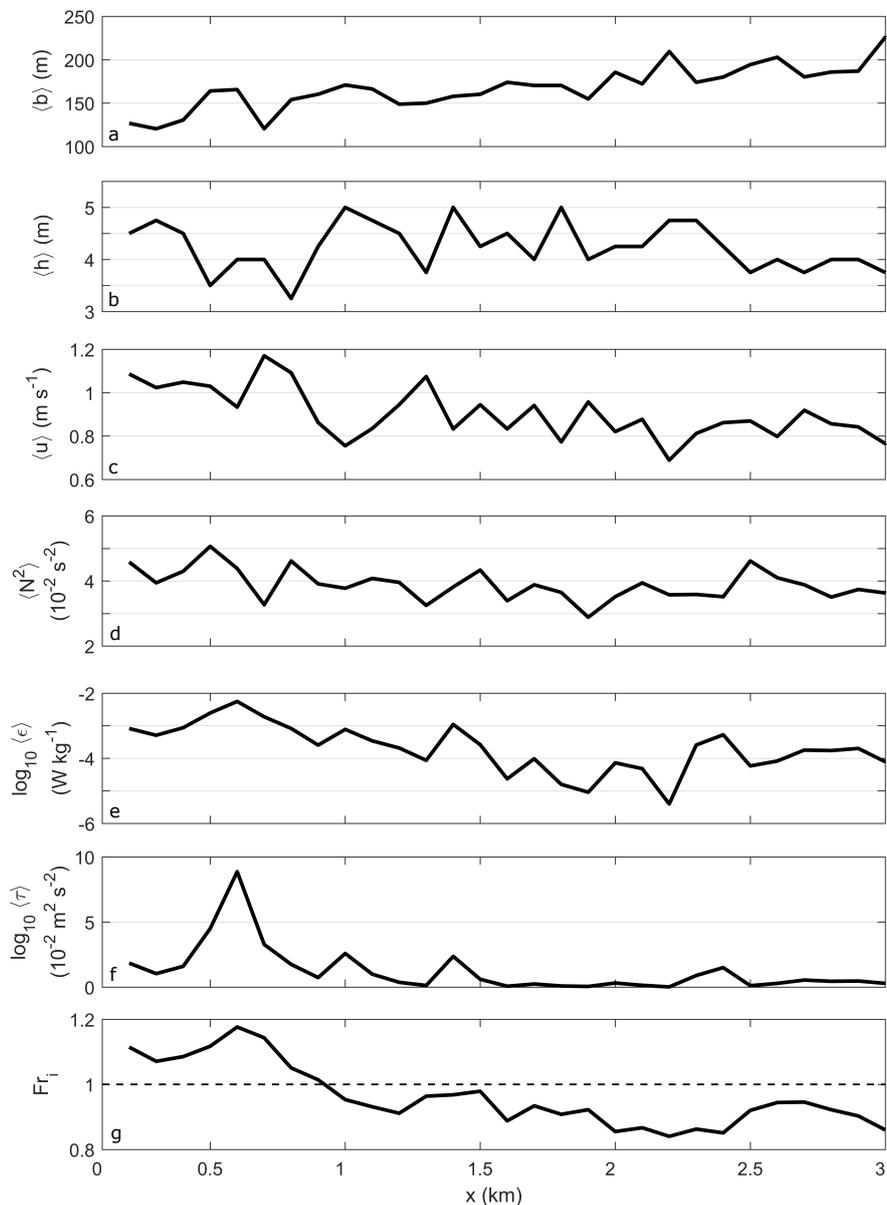
Figure 6. The evolution of plume-averaged quantities with distance from tailrace discharge point. (a) Plume width $\langle b \rangle$, (b) surface layer thickness $\langle h \rangle$, (c) along-channel velocity $\langle u \rangle$, (d) stratification $\langle N^2 \rangle$, (e) dissipation rate $\langle \epsilon \rangle$, (f) internal turbulence stress $\langle \tau \rangle$ and (g) internal Froude number (Fr_i). The dashed line in (g) is the critical value $Fr_i = 1$. Each term was averaged over the depth of the surface layer (h). These values are from one along-channel transect on 07 March 2016 and representative of the plume behaviour observed during all transects.
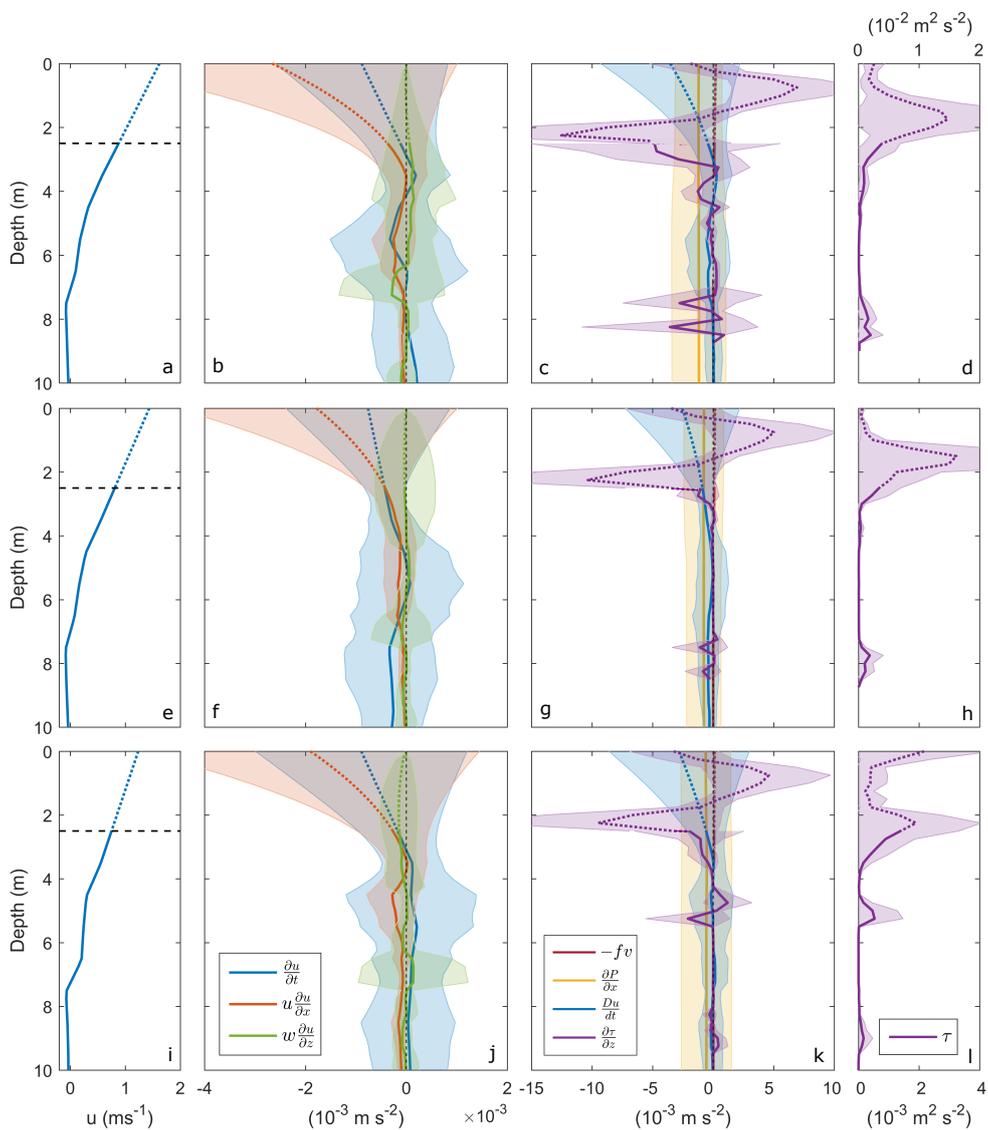
Figure 7. Terms in the along-channel momentum budget averaged over $0 \leq x < 1$ km (top row), $1 \leq x < 2$ km (middle) and $2 \leq x < 3$ km (bottom). Profiles of (a,e,i) along-channel velocity u (dashed lines indicate depth over which velocity was interpolated to the surface), (b,f,j) local acceleration (blue) and advection (x and z-component, orange and green respectively), (c,g,k) Coriolis force (red), pressure gradient (yellow), total acceleration (blue) and turbulence stress divergence (purple), and (d,h,l) internal turbulence stress (τ, purple). The shading around each profile represents one standard deviation. The dotted profile above 2.5 m for each term indicates the region over which each variable was calculated using interpolated velocity data.

Turbulence stress was surface-intensified, exceeding $\tau = -10^{-2}$ m^{2}s^{-2} at the base of the plume (Fig. 7d). This maximum value is over one order of magnitude greater than peak τ within the Columbia River (Kilcher et al., 2012). The positive stress in

195 the surface 2 m indicates the movement of momentum downwards from the near-surface, where τ was an order of magnitude weaker, to the base of the surface layer at 4 m. Below the surface layer, τ tended towards zero with depth. This resulted in large stress divergence within the surface layer and a large decrease in $\partial\tau/\partial z$ below 4 m (Fig. 7c).

Further downstream ($1 \leq x < 2$ km) the total deceleration was principally within the surface layer (Fig. 7g), driven by the along-channel advection component and local acceleration (Fig. 7f). Below the plume, Du/Dt tended towards zero. The

200 pressure gradient was approximately half the magnitude of Du/Dt within the surface layer and comparable to Du/Dt below the plume. Maximum $\tau = 10^{-3}$ m^{2}s^{-2} at the base of the plume was an order of magnitude greater than τ within the plume while, below the surface layer, τ tended to zero and was relatively constant which agrees with the weak deceleration observed (Fig. 7g,h). The high interfacial stress and weak ambient τ resulted in large stress divergence within the surface layer and a decrease in $\partial\tau/\partial z$ towards zero below 3 m (Fig. 7g).

205 Towards the seaward end of Deep Cove ($2 \leq x \leq 3$ km) the along-channel advection component remained strong and dominated the near-surface deceleration (Fig. 7j). Below 4 m, the weaker advection and spreading components balanced $\partial u/\partial t$ which led to a relatively steady ambient (Fig. 7k). The maximum pressure gradient was an order of magnitude less than Du/Dt and relatively constant with depth. The stress at $z = 0$ was comparable to the maximum τ at the base of the plume (Fig. 7l), indicating that wind may have contributed a force to the surface layer at the seaward end of Deep Cove. This resulted in a

210 surface-intensified stress divergence that reduced to zero with depth (Fig. 7k).

4 Discussion

4.1 Comparison of tailrace inflow with river discharges

The buoyant discharge into the head of Deep Cove is comparable to inflows of other coastal river plumes in many ways. The surface plume flowed at speeds greater than 1.5 ms^{-1} (Fig. 5b) which is consistent with the high flow speeds of the Columbia

215 River (Kilcher et al., 2012) and the Fraser River (Tedford et al., 2009). However, the discharge rates of these other plumes are over one order of magnitude greater than the maximum $Q = 550$ m^{3}s^{-1} in Deep Cove, where high inflows of $Q = 17,000$ and $10,000$ m^{3}s^{-1} have been recorded for the Columbia (McCabe et al., 2009) and Fraser Rivers respectively (MacDonald and Horner-Devine, 2008). Studies of river plumes of a comparable discharge rate to the tailrace inflow, such as the Merrimack and Connecticut River, exhibit mean flow rates which are generally half the speed of the plume in Deep Cove (O'Donnell et al.,

220 2008; Chen et al., 2009).

The combination of high plume velocities and strong stratification, due to the continuous freshwater inflow to Deep Cove and substantial annual rainfall, resulted in active turbulent mixing of the plume and ambient waters. The maximum stratification at the base of the plume ($N^2 = 10^{-1}$ s^{-2}) (Fig. 5c) was approximately one order of magnitude greater than N^2 observed in the Columbia River during periods of large freshwater flux (Kilcher et al., 2012). Within the near-field region in Deep Cove, the

225 highly stratified interfacial layer supported the intense shear generated by the high plume speeds, resulting in surface-intensified

turbulence ($\epsilon > 10^{-3}$ Wkg^{-1}) (Fig. 6e) at least one order of magnitude larger than maximum ϵ measured in other river plumes of a comparable size (MacDonald et al., 2007; O'Donnell et al., 2008). The mean ϵ in the near-field of Deep Cove is instead comparable to the highest values recorded in other much larger river plume settings. Both the Fraser and Columbia Rivers displayed maximum $N^2 = 10^{-2}$ s^{-2} at the base of their respective surface layers and the velocity shear across the pycnoclines

230 resulted in peak $\epsilon > 10^{-4}$ Wkg^{-1} (MacDonald and Geyer, 2004; Kilcher et al., 2012). Therefore, the tailrace discharge into Deep Cove exhibits flow properties that are comparable to much larger river systems and the near-field region of Deep Cove is amongst the most strongly stratified and turbulent in coastal regimes.

4.2 The balance of the momentum budget

The vertical structure of the momentum budget components vary significantly between the distinct layers of the upper water

235 column (i.e., the surface plume, shear-stratified interface and ambient below) (Fig. 7). Therefore, the balance of the components of Eq. (3) in the Deep Cove system, as illustrated in Fig. 8, were examined within each of these layers. The sum of the momentum budget terms averaged over the surface plume layer was approximately zero (Fig. 9d) therefore, the budget was closed and a balance was achieved within the plume. The dynamical balance existed between Du/Dt and $\partial\tau/\partial z$, where Du/Dt was dominated by along-channel advection with a further, albeit weaker, contribution by the local acceleration term

240 (Fig. 9a). The near-surface along-channel advection was greatest at the tailrace discharge point (10^{-3} ms^{-2}) where maximum plume speeds were observed and generally decreased with distance, tending towards zero as the flow speeds decreased (Fig 6c). The pressure gradient, approximately half the magnitude of the along-channel advection component, also acted to increase the total deceleration to balance the internal stress divergence. The overall balance between plume deceleration and turbulent stress divergence over the length of Deep Cove signifies that the vertical flux of low momentum, dense water into the freshwater

245 surface layer controlled the deceleration of the river plume from the tailrace discharge point to as far as 3 km downstream. This balance of terms, where shear-driven turbulence acted as the primary driver of plume deceleration, has been previously observed in the near-field region of river plumes elsewhere (McCabe et al., 2009; Kilcher et al., 2012).

In the quiescent ambient below the surface layer ($h \leq z < 10$ m), a balance of momentum was also achieved (Fig. 9d). The momentum budget was dominated by the pressure gradient and the advection term without rotation, which is almost negligible

250 (Fig. 9c); i.e., the Bernoulli principle. The spreading component was approximately half the magnitude of the along-channel advection term in the ambient and contributed to the total deceleration. Between $4 - 10$ m, τ was relatively constant (10^{-5} ms^{-2}) (Fig. 7d), linked to the reduced turbulent mixing at these depths (Fig. 5e), thus the stress divergence became negligible in the ambient (Fig. 9c).

However, the budget components averaged over the shear-stratified interfacial layer ($2 \leq z < h$ m) show that an along-

255 channel momentum balance was not obtained within the interface (Fig. 9d). The sum of the budget terms was negative as a result of weak deceleration ($Du/Dt < 0$) and a strong negative stress divergence term (Fig. 9b). In the initial 1 km downstream of the discharge point, there was no positive budget component within the interface and the total momentum exceeded -5×10^{-3} ms^{-2} before tending towards zero farther downstream. This discrepancy in the budget signifies that the input of momentum required to balance the output, primarily driven by turbulence, was not present within the interfacial layer. There are a number
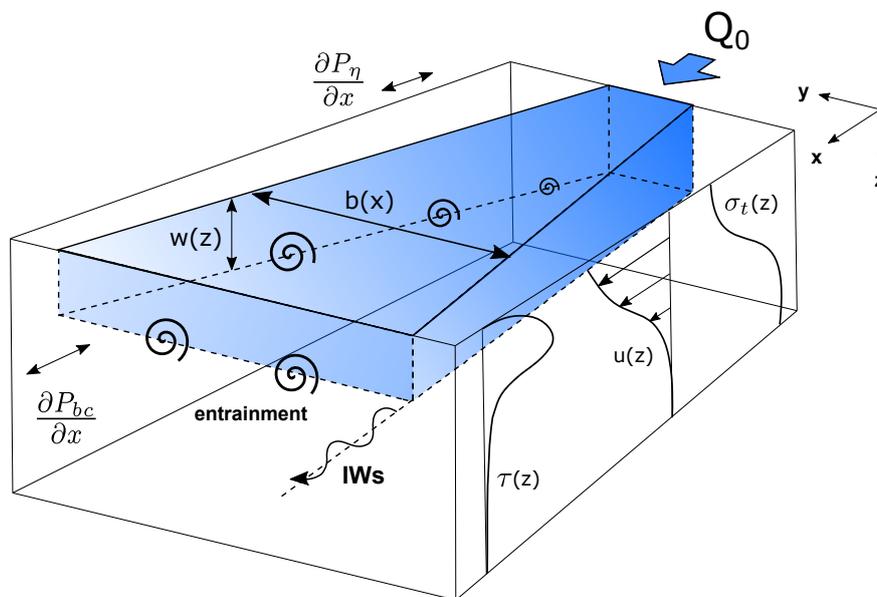
Figure 8. Schematic representation of the terms in the along-channel plume momentum budget, including near-field vertical structure. The plume is the blue shaded box fed by inflow Q_0. The increasing width of the plume in the across-channel direction is b and the decreasing thickness of the plume is h. Vertical profiles of sigma-t (σ_t), along-channel velocity (u) and turbulence stress (τ) are shown. The baroclinic (P_{bc}) and barotropic (P_η) components of pressure and the vertical entrainment velocity (w) are indicated. Entrainment between the plume and ambient is illustrated and internal waves (IWs) propagate along the base of the pycnocline.

260   of possible sources for this discrepancy. Firstly, the budget components were not fully resolved by the observations. Secondly, errors in the control volume technique arose from invalid assumptions (see Kilcher et al. (2012) for further details). Thirdly, other processes, which were not accounted for in Eqn. 3, impacted the momentum balance within the interface of the Deep Cove system.

The influence of other riverine physical processes, not resolved by the budget, on the momentum of the system is now
265   considered. To balance the negative $\partial\tau/\partial z$ (Fig. 9b), a positive Du/Dt is required. Return flows are intrinsic to estuarine circulation and propagate in the opposite direction of the plume between the surface layer and ambient below (Pritchard, 1952). The up-fjord directed current would transport momentum back into the system along the pycnocline. In order to balance the observed $\partial\tau/\partial z = -10^{-3}$ ms^{-2} within the interface, the return flow would have to increase by approximately 0.9 ms^{-1} from the seaward end of Deep Cove to the tailrace discharge point. This is more than four times greater than the difference of ~ 0.2
270   ms^{-1} between return flow velocities at either end of Deep Cove measured by O'Callaghan and Stevens (2015). Therefore, a return flow would not be sufficient to contribute the additional up-stream momentum required to balance the budget terms in the interface.
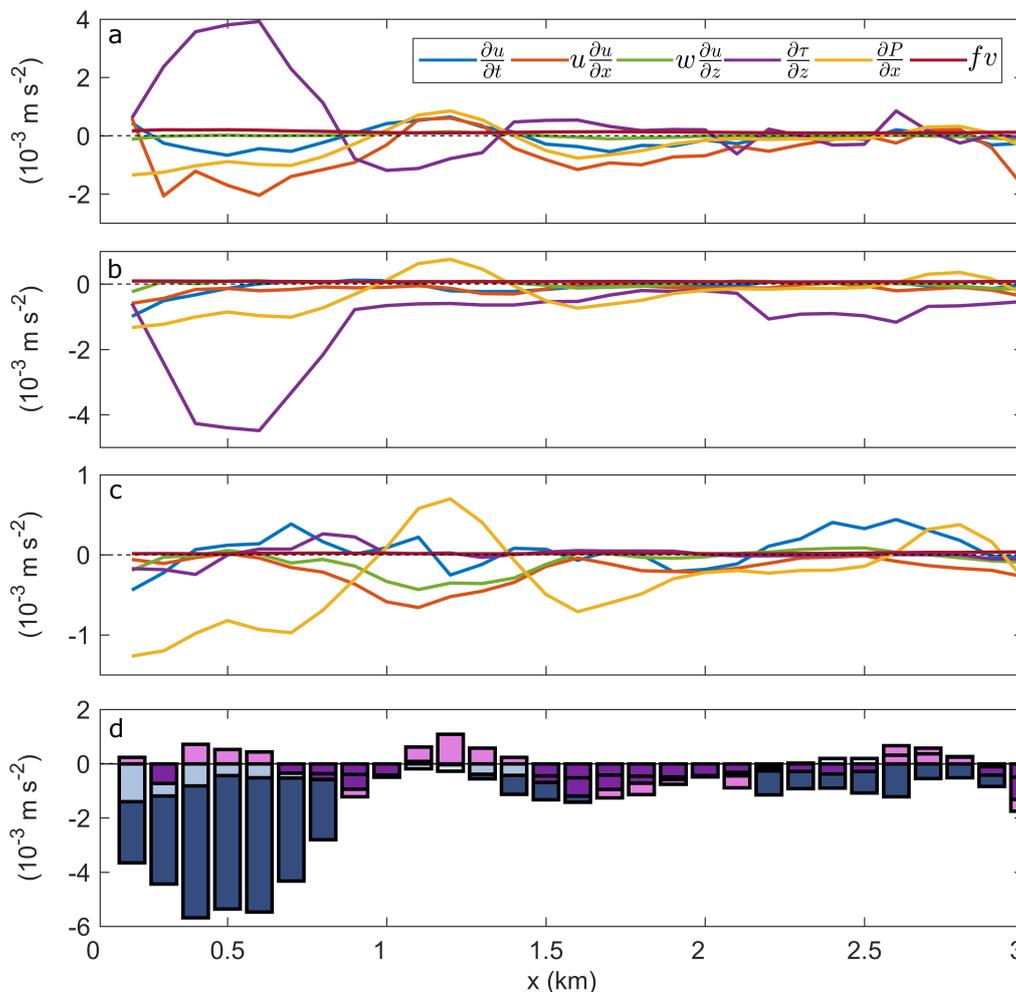
Figure 9. The terms in the along-channel momentum budget averaged over the depth of (a) the plume ($0 \leq z < 2$ m), (b) the interface ($2 \leq z < h$ m), where h is defined in Fig. 6b, and (c) below the surface layer ($h \leq z < 10$ m), and (d) the sum of all the momentum components within the plume (pink), interface (light blue) and below the surface layer (dark blue).

4.3 The role of internal waves in the shear-stratified layer

The complex density interfaces and turbulence in the surface layer are clearly illustrated in the high intensity acoustic backscat-

275 ter from the measurements by the shipboard echosounder (Fig. 4). The momentum within the near-surface plume is transferred downwards by turbulence to the base of surface layer however, does not remain in the shear-stratified interfacial layer. The momentum is instead transferred away from the interface. The sounder shows internal waves propagating along the base of the

surface layer which are capable of redistributing significant quantities of energy contained below the plume farther downstream (Nash and Moum, 2005).

280   The spectral distribution of temperature within the interfacial layer was inferred from the near-field mooring approximately 1 km downstream from the tailrace discharge point (Fig. 1c). The tidal signal, representing approximately 12% of the total energy in the signal, was filtered from the temperature data using classical harmonic analysis (T_TIDE, Pawlowicz et al. (2002)). The time series was then split into half-overlapping intervals equivalent to the inertial frequency and the spectrum was computed using Welch's periodogram method. The spectral fall-off rate of the signal varied with frequency (Fig. 10). A spectral slope

285   of σ^{-2} ('-2' on a log-log scale) was observed throughout the low-frequency range of the internal wave band ($\sigma < 4f$ cpd). For the higher frequency range ($10^2 < \sigma < N$ cpd), the continuum internal wave band power spectra sloped at -5/3 which suggests a mean dominance of shear-induced turbulence. This transition to a weaker slope, instead of the signal following the steeper -2 slope from lower frequencies, indicates that there is a large amount of energy contained at these high frequencies. The smooth spectral slope of -2 within the continuum internal wave band is consistent with the background canonical GM

290   spectrum of internal waves in the open ocean Garrett and Munk (1972), which suggests that internal waves could be one of the high-frequency processes that are captured by the energetic spectrum. The sounder transect illustrates their existence in this system. It is these internal waves which could be an unresolved process in the momentum budget, thus responsible for the balance within the shear-stratified interface not being closed using Eqn. 3 alone.

       Further evidence of the existence of internal waves is the observed transition from a supercritical ($Fr_i > 1$) to sub-critical

295   ($Fr_i < 1$) flow regime at approximately 1 km downstream from the tailrace discharge point (Fig. 6g). The free propagation of internal waves during this change in flow regime have been identified at other plume fronts (Nash and Moum, 2005; Jay et al., 2009; Pan and Jay, 2009; Kilcher et al., 2010; Osadchiev, 2018). Illustrated as variability in the acoustic scattering along the density interface in the sounder transect (Fig. 4), the variability in plume thickness and plume speed (Fig. 6b,c), which was not induced by a change in discharge rate (Fig. 2a), was also consistent with internal wave release (Kilcher et al., 2010). Note that

300   the observed internal waves at $x = 0.8$ km in the echosounder transect (Fig. 4) occurred when near-surface plume speeds were ~ 0.1 ms^{-1} weaker than when the along-channel transect in Fig. 6 was conducted. Therefore, the transition in Froude number would occur closer to the tailrace discharge point than when plume speeds were higher during the transect illustrated in Fig. 6g.

       Internal waves were also observed propagating along the base of the interfacial layer at Elizabeth Island, approximately 5

305   km downstream of the tailrace discharge point (Fig. 11). The freshwater surface layer is relatively well-mixed and observed as the dark backscatter from the water surface to approximately 1.5 m deep. The highly stratified ($N^2 > 0.4$ s^{-2}) base of the interfacial layer is evident as the dark band at 3 m depth. Below the interface, internal waves can be seen propagating at approximately 5 m depth. The echosounder transects in both the near-field (Fig. 4) and far-field plume region (Fig. 11), the transition between flow regimes (Fig. 6g), and the energetic high-frequency band of the temperature spectrum (Fig. 10),

310   provide clear evidence of the existence of internal waves propagating along the shear-stratified interfacial layer.

       Strong stratification is favourable for the generation and propagation of internal waves and the N^2 observed here is amongst the highest recorded in the coastal ocean. The total vertical momentum flux divergence ($\partial F_z / \partial z$) of internal gravity waves was
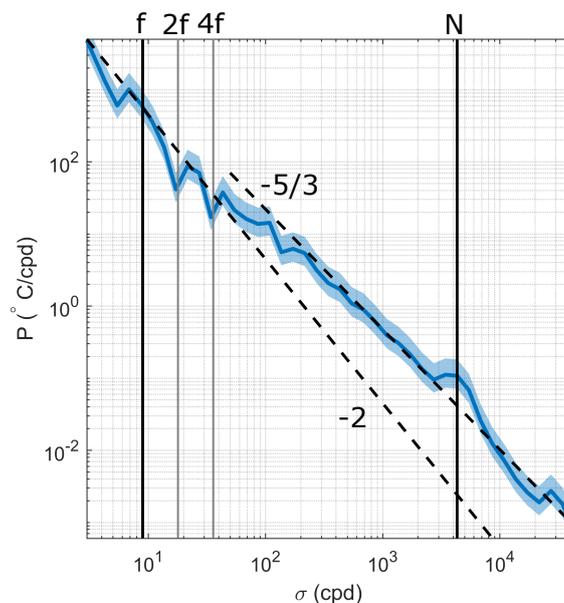
Figure 10. Spectral analysis of temperature in the interface (3.5 m) for the entire mooring time series, split into half-overlapping intervals equivalent to the inertial frequency (20 degrees of freedom) and the spectrum was computed using Welch's periodogram method. The focus is on the [f,N] range with particular frequencies highlighted. For reference, spectral slopes of -2 and -5/3 are indicated by the black dashed lines and a 95% confidence interval is the shaded region around the spectrum.

calculated, using Eqn. 2, to be $F_z = 1.75 \times 10^{-4}$ $\mathrm{m^2s^{-2}}$. Thus the momentum flux divergence $\partial F_z/\partial z = 1.65 \times 10^{-4}$ $\mathrm{ms^{-2}}$. This equates to approximately 14.9% of the total measured momentum (Fig. 9) which suggests that, by removing energy along

315   the pycnocline, internal waves could be an important mechanism of momentum transport within the shear-stratified interface.

4.4 Momentum loss in the shear-stratified layer

As well as allowing for the release of internal waves, the transition from a supercritical to sub-critical flow regime in the initial 1 km (Fig. 6g) also indicates the presence of an internal hydraulic jump (Cummins et al., 2006). Hydraulic jumps have previously been observed in Deep Cove, caused by variable discharge rates, as the fast surface plume discharged into the

320   deep, stationary ambient presents an ideal environment for their generation (O'Callaghan and Stevens, 2015). These jumps can alter the vertical structure of the stratified flow by intensifying density gradients, accelerating the flow and modifying vertical shear (Nash and Moum, 2001). At the jump location in Deep Cove, an increase in plume thickness from 3.3 m to 5 m (Fig. 6b) indicates where the thin near-surface supercritical flow is matched to the thicker sub-critical layer. Furthermore, jump-occurrence was corroborated by intense turbulence dissipation in the near-surface ($\epsilon > 10^{-3}$ $\mathrm{Wkg^{-1}}$) (Fig. 6e). When

325   flow dominated by kinetic energy (a supercritical flow) transitions into a flow dominated by its potential energy (a sub-critical
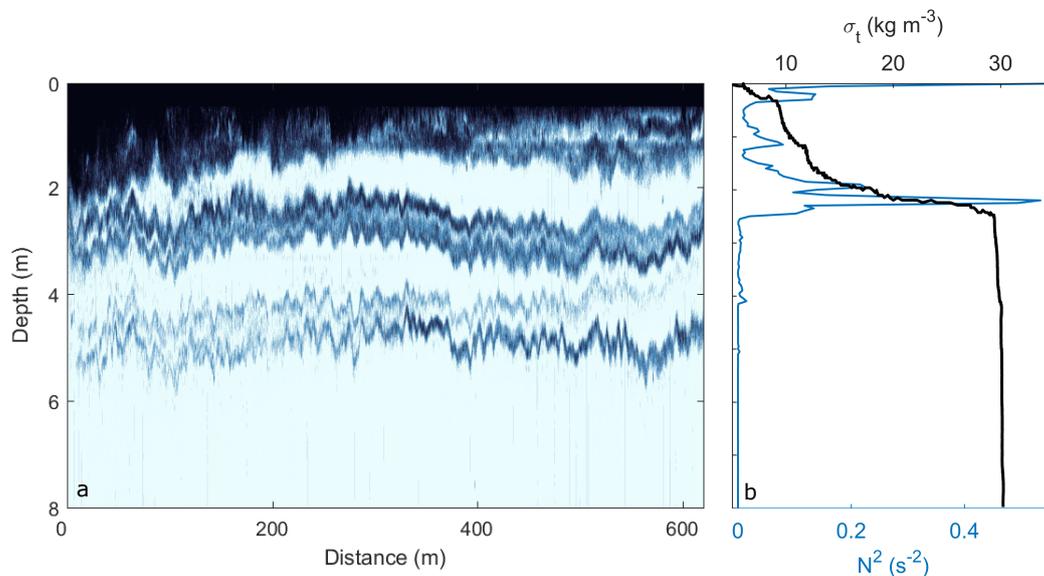
Figure 11. (a) Along-channel echosounder (EK60) transect from beside Elizabeth Island, with surface flow moving seaward from left to right and (b) vertical $\sigma - t$ (black) and buoyancy frequency-squared (blue) profiles from the VMP at the same location. Elizabeth Island is approximately 5 km downstream of the tailrace discharge point.

flow), mechanical energy is released and is either radiated away by internal waves or dissipated locally (Nash and Moum, 2001; Klymak et al., 2004; Osadchiev, 2018).

The power dissipated across a hydraulic jump can be estimated from $E = \rho g' Q \Delta H$ where Q is the tailrace discharge rate and $\Delta H = (y_2 - y_1)^3/4y_2 y_1$ (Weber, 2001). The depths for the surface plume and Deep Cove are $y_1 = 10$ m and $y_2 = 110$

330   m respectively, reflecting the difference between the depth of the surface layer and the inner fjord, thus $\Delta H = 225$ m. When $Q = 530 \, \mathrm{m^3 s^{-1}}$, a total of $E \sim 28.7$ MW is dissipated across the jump. This is the equivalent to over 30 % of the total energy within the interface. A more conservative depth estimate for the supercritical and sub-critical layers of $y_1 = 2$ m and $y_2 = 10$ m respectively, as it is unlikely for the hydraulic jump to fill the entire water column, results in a total energy loss of 2 % across the hydraulic jump. Therefore, the hydraulic jump contributed to up to one third of the total dissipation of momentum within

335   the interfacial layer and is thus a crucial, yet generally unconsidered, process in the balance of plume momentum.

5   Conclusions

The momentum budget constructed here using hydrographic and turbulence observations, integrated over a control volume, illustrates the role of each of the budget components on the distribution of momentum within the near-field region of a buoyant plume (Fig. 8). Using direct measurements of ϵ from the vertical microstructure profiles to calculate τ, hence more accurately

Ocean Science
Discussions

EGU

340   representing the mechanisms of turbulent mixing, is a development of the control volume technique established by MacDonald
and Geyer (2004) which indirectly inferred τ from the residual of the budget components.

The influence of the budget components on near-field plume structure and evolution varied between the surface plume
layer, the shear-stratified interfacial layer, and the quiescent ambient below. Within the plume, the turbulence stress divergence
controlled the deceleration of the plume for as far as 3 km downstream from the discharge point by entraining low-momentum
345   ambient water into the surface layer; i.e., Du/Dt balanced $\partial\tau/\partial z$ (Fig. 9a). The total plume deceleration and adverse pressure
gradient, approximately half the magnitude of Du/Dt, was also required to balance the stress divergence. This result directly
confirms the control volume technique first applied by MacDonald and Geyer (2004) and validated by Kilcher et al. (2012).

Within the interfacial layer however, a balance of momentum using the budget terms was not achieved: there was no corre-
sponding input of momentum to balance the output driven primarily by turbulence (Fig. 9b). This discrepancy in the momentum
350   budget of the interfacial layer could be a result of the invalidity of control volume assumptions, the observations not fully re-
solving the budget components, or other unresolved physical processes. A transition from a supercritical to sub-critical flow
regime in the initial 1 km (Fig. 6f) induced an internal hydraulic jump which modified both the plume flow speeds and the
vertical structure, and was capable of dissipating between 2 - 30 % of the total energy within the interface. The subsequent
release of internal waves, visible propagating along the base of the surface layer in both near and far-field plume regions (Fig. 4,
355   11) were also capable of transporting almost 15 % of the total energy out beyond the plume's boundaries. The generation of in-
ternal waves by river plumes and their transport of energy and momentum along the pycnocline has been previously observed
in both large and small river systems (Nash and Moum, 2005; Pan and Jay, 2009; Osadchiev, 2018). Thus the momentum
within the system which was not resolved by the budget and Eqn. 3 could be accounted for by considering the redistribution
and dissipation of momentum by these processes. The consideration of internal hydraulics and wave radiation when evaluat-
360   ing a momentum budget in a shear-stratified environment is therefore necessary to fully understand the impact of governing
dynamics on plume behaviour and evolution.

It is anticipated that this work, which is directly applicable to the near-field plume region of a river entering the ambient
ocean, can also be applied to other estuarine and coastal regimes, as well as stratified shear flows. The rapid river inflows into the
coastal ocean can strongly influence both the structure and mixing dynamics of the plume, while the internal wave generation
365   and transports impact the physical, chemical and biological structure and processes in the larger scale coastal environment.
Improved understanding of the dynamics and energetics in this system will enable better predictions of the ultimate fate of the
freshwater discharge, materials and energy.

Ocean Science
Discussions

Ocean Science
Discussions

EGU

Open Access

References

Bowman, M., Dietrich, D., and Mladenov, P. (1999). Predictions of circulation and mixing in Doubtful Sound, arising from variations in runoff and discharge from the Manapouri power station. Volume 56 of *Coastal and Estuarine Studies*. American Geophysical Union, Washington, D. C.

Chen, F. and MacDonald, D. G. (2006). Role of mixing in the structure and evolution of a buoyant discharge plume. *Journal of Geophysical Research*, 111(C11):C11002.

Chen, F., MacDonald, D. G., and Hetland, R. D. (2009). Lateral spreading of a near-field river plume: Observations and numerical simulations. *Journal of Geophysical Research: Oceans*, 114(C7):C07013.

Cummins, P. F., Armi, L., and Vagle, S. (2006). Upstream internal hydraulic jumps. *Journal of Physical Oceanography*, 36(5):753–769.

Fong, D. A., and Geyer, W. R. (2002). The alongshore transport of freshwater in a surface-trapped river plume. *Journal of Physical Oceanography*, 32(3):957–972.

Garrett, C., and Munk, W. (1972). Space-Time scales of internal waves. *Geophysical Fluid Dynamics*, 3(1):225–264.

Geyer, W. R., Ralston, D. K., and Holleman, R. C. (2017). Hydraulics and mixing in a laterally divergent channel of a highly stratified estuary. *Journal of Geophysical Research: Oceans*, 122(6):4743–4760.

Hetland, R. D. (2005). Relating river plume structure to vertical mixing. *Journal of Physical Oceanography*, 35(9):1667–1688.

Hetland, R. D. (2010). The effects of mixing and spreading on density in near-field river plumes. *Dynamics of Atmospheres and Oceans*, 49(1):37–53.

Hunter, E. J., Chant, R. J., Wilkin, J. L., and Kohut, J. (2010). High-frequency forcing and subtidal response of the Hudson River plume. *Journal of Geophysical Research*, 115(C7):C07012.

Jay, D. A., Pan, J., Orton, P. M., and Horner-Devine, A. R. (2009). Asymmetry of Columbia River tidal plume fronts. *Journal of Marine Systems*, 78(3):442–459.

Kakoulaki, G., MacDonald, D., and Horner-Devine, A. R. (2014). The role of wind in the near field and midfield of a river plume. *Geophysical Research Letters*, 41(14):5132–5138.

Kilcher, L. F., and Nash, J. D. (2010). Structure and dynamics of the Columbia River tidal plume front. *Journal of Geophysical Research*, 115(C5):C05S90.

Kilcher, L. F., Nash, J. D., and Moum, J. N. (2012). The role of turbulence stress divergence in decelerating a river plume. *Journal of Geophysical Research: Oceans*, 117(C5):C05032.

Klymak, J. M., and Gregg, M. C. (2004). Tidally generated turbulence over the Knight Inlet Sill. *Journal of Physical Oceanography*, 34(5):1135–1151.

MacDonald, D. G. and Geyer, W. (2004). Turbulent energy production and entrainment at a highly stratified estuarine front. *Journal of Geophysical Research*, 109(C5):C05004.

MacDonald, D. G., Goodman, L., and Hetland, R. D. (2007). Turbulent dissipation in a near-field river plume: A comparison of control volume and microstructure observations with a numerical model. *Journal of Geophysical Research*, 112(C7):C07026.

MacDonald, D. G. and Horner-Devine, A. R. (2008). Temporal and spatial variability of vertical salt flux in a highly stratified estuary. *Journal of Geophysical Research*, 113(C9):C09022.

MacDonald, D. G. and Chen, F. (2012). Enhancement of turbulence through lateral spreading in a stratified-shear flow: Development and assessment of a conceptual model. *Journal of Geophysical Research: Oceans*, 117(C5):C05025.

MacDonald, D. G., Carlson, J., and Goodman, L. (2013). On the heterogeneity of stratified-shear turbulence: Observations from a near-field river plume. *Journal of Geophysical Research: Oceans*, 118(11):6223–6237.

McCabe, R. M., Hickey, B. M., and MacCready, P. (2008). Observational estimates of entrainment and vertical salt flux in the interior of a 415 spreading river plume. *Journal of Geophysical Research*, 113(C8):C08027.

McCabe, R. M., MacCready, P., and Hickey, B. M. (2009). Ebb-tide dynamics and spreading of a large river plume. *Journal of Physical Oceanography*, 39(11):2839–2856.

McPherson, R. A., Stevens, C. L., and O'Callaghan, J. M. (2019). Turbulent scales observed in a river plume entering a fjord. *Accepted to Journal of Geophysical Research: Oceans*.

Nash, J. D., and Moum, J. N. (2001). Internal hydraulic flows on the continental shelf: High drag states over a small bank. *Journal of 420 Geophysical Research: Oceans*, 106(C3),4593–4611.

Nash, J. D., and Moum, J. N. (2005). River plumes as a source of large-amplitude internal waves in the coastal ocean. *Nature*, 437(7057),400–403.

O'Callaghan, J. M. and Stevens, C. L. (2015). Transient river flow into a fjord and its control of plume energy partitioning. *Journal of 425 Geophysical Research: Oceans*, 120(5):3444–3461.

O'Donnell, J., Ackleson, S. G., and Levine, E. R. (2008). On the spatial scales of a river plume. *Journal of Geophysical Research*, 113(C4):C04017.

Osadchiev, A. A. (2018). Small Mountainous Rivers Generate High-Frequency Internal Waves in Coastal Ocean. *Scientific Reports*, 8(1):16609.

Pan, J. and Jay, D. A. (2009). Dynamic characteristics and horizontal transports of internal solitons generated at the Columbia River plume 430 front. *Continental Shelf Research*, 29(1):252–262.

Pickard, G. L. and Stanton, B. R. (1980). *Pacific fjords - A review of their water characteristics*, pages 1–51. Springer US, Boston, MA.

Pawlowicz, R., Beardsley, B., and Lentz, S. (2002). Classical tidal harmonic analysis including error estimates in MATLAB using T_TIDE. *Computers and Geosciences*, 28(8):929–937.

Pritchard, D. W. (1952). Estuarine Hydrography. *Advances in Geophysics*, Vol.1, Academic Press, 243–280

Tedford, E. W., Carpenter, J. R., Pawlowicz, R., Pieters, R., and Lawrence, G. A. (2009). Observation and analysis of shear instability in the Fraser River estuary *Journal of Geophysical Research*, 114(C11):C11006

Walters, R. A., Goring, D. G., and Bell, R. G. (2001). Ocean tides around New Zealand. *New Zealand Journal of Marine and Freshwater Research*, 35(3):567–579.

Weber, L.J. (2001). The hydraulics of open channel flow: An introduction. *Journal of Hydraulic Engineering*, 127(3):246–247.

Yankovsky, A. E., Hickey, B. M., and Münchow, A. K. (2001). Impact of variable inflow on the dynamics of a coastal buoyant plume. *Journal of Geophysical Research: Oceans*, 106(C9):19809–19824.